The 2020 International Power Electronics and Motion Conference (IPEMC 2020 ECCE Asia)

Modulation Considerations for Modular Multilevel Converter Operating with Parallel Branches and Phase-Shifted Carriers

S. Milovanovic and D. Dujic

POWER ELECTRONICS LABORATORY
ÉCOLE POLYTECHNIQUE FÉDÉRALE DE LAUSANNE

Modulation Considerations for Modular Multilevel Converter Operating with Parallel Branches and Phase-Shifted Carriers

Stefan Milovanović, *Student Member, IEEE,* Dražen Dujić, *Senior Member, IEEE*
Power Electronics Laboratory, École Polytechnique Fédérale de Lausanne
stefan.milovanovic@epfl.ch; drazen.dujic@epfl.ch

***Abstract*—The branch paralleling represents one of the available options with regards to the modular multilevel converter power extension. In such a case, the main technical challenge resides in the control domain, whereas a new set of possibilities from the voltage modulation standpoint becomes available along the way. This paper provides a thorough mathematical analysis of the modular multilevel converter operating with parallel branches and utilizing phase-shifted carrier modulation to synthesize the desired voltage references. The influence of the adjacent branches' carriers shift on the voltages across the terminals of the converter leg is presented in a comprehensive manner. Detailed simulations confirm the derived mathematical predictions and allow for the performance guided choice of relevant modulator parameters.**

***Index Terms*—modular multilevel converter, medium voltage high power conversion, power extension, branch paralleling, PWM, phase-shifted carriers**

I. Introduction

The effortless fulfillment of an application voltage requirements, by means of stacking the so-called submodules (SMs) in series, paved the way for the Modular Multilevel Converter (MMC) in the field of High Voltage (HV) and Medium Voltage (MV) conversion [1]–[3]. **Fig. 1a** depicts the MMC phase leg comprising two branches, each consisting of N series connected SMs, found most commonly in either Half-Bridge (HB) or Full-Bridge (FB) configuration, and an inductor L_{br}. High-quality AC voltage waveforms can be obtained, resulting in a very modest or even no additional filtering requirements of the converter AC currents.

The essential part of any MMC design implies distinctly defined SM ratings. For a fixed current rating of the SMs, stacking more of them in series increases the MMC voltage handling capabilities. As a result, the converter rated power increase can be achieved as long as the application voltage is to be freely chosen. Point-to-point UHVDC systems [4], where substantial power ratings are achieved through rising the transmission line voltages even above $1\mathrm{MV}$ [5], can be said to match such a power increase philosophy. However, the power increase of a converter operating at the strictly defined voltage class (e.g. $15\mathrm{kV}$) implies the boost of its current handling capabilities. Hydro applications [6], where power ratings of several hundreds of mega-watts are achieved at the voltage level of approximately $25\mathrm{kV}$, owing to the generator voltage limitations, can be considered a good example of such a case.

Fig. 1b demonstrates the change in the converter leg structure should paralleling of the branches be employed with the aim of extending the power capacity of the converter [7]. In order to retain the naming consistency, what has been referred to as the branch in the conventional MMC will henceforth be referred to as the Sub-Branch (SBR). A thorough analysis of the control of the MMC operating in this structure was conducted in [7]. An advantage of the power extension method depicted in **Fig. 1b** refers to the quality of voltage generated by a set of parallel SBRs as a whole. Compared to the conventional MMC leg depicted in **Fig. 1a**, paralleling of the SBRs introduces an additional degree of freedom from the leg voltage generation standpoint. In case Phase Shifted Carrier (PSC) modulation is used to synthesize the branch reference voltages, introduction of the shift among the SBR carrier sets affects the converter terminal voltages. This paper provides a thorough mathematical analysis on this matter and its main contributions can be summarized as:

- Complete mathematical derivation of the frequency components appearing in the spectrum of both AC and DC voltages of the MMC operating with an arbitrary number of parallel SBRs is provided. As all the results are presented in a general form, they are applicable to any chainlink converter. Moreover, while the existing literature present the spectral content analysis of the conventional MMC featuring the open-loop control, this paper, for the first time, considers the modulation index generation in a closed-loop manner.
- Analysis of the available degrees of freedom at the modulator level is conducted explaining the trade-offs between the quality of voltage seen from the AC and DC ports of an observed converter leg.
- A set of detailed simulation models confirms and validates the theoretical developments presented throughout the paper.

II. The Available degrees of freedom

Henceforward, without the loss of generality, the use of HB SMs will be assumed, whereas the operation relying on the use of PSC modulation will be considered. At first instance, setting the phase shift between two carriers modulating two adjacent SMs within an observed (sub)branch as $\gamma_{\mathrm{c}} = 2\pi/N$ seems to be natural and popular choice [8], [9]. Since the purpose of

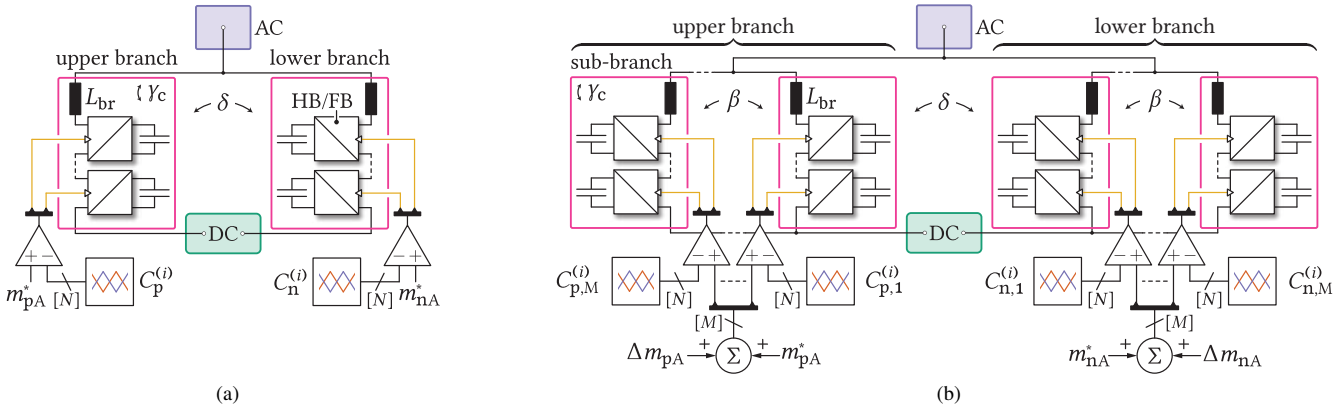

Fig. 1. (a) Leg of the conventional MMC; (b) Leg of the MMC comprising multiple parallel SBRs;

stacking the SMs in series is generating the multilevel voltage waveforms, this phase shift will be considered fixed and not a degree of freedom. To commence the analysis, one can observe the conventional MMC leg, presented in **Fig. 1a**. According to [8], [9], carriers of two identically indexed SMs belonging to the upper and lower branch, respectively, can be phase-shifted as

$$C^{(i)}_{\mathrm{p}} = C^{(i)}_{\mathrm{n}}(\omega_{\mathrm{c}}t - \delta), \tag{1}$$

where $\omega_{\mathrm{c}} = 2\pi f_{\mathrm{c}}$ denotes the carrier angular velocity, while the subscripts "p" and "n" denote the upper and lower branch quantities, respectively. The proper selection of angular displacement δ, leads to a possible increase in the number of voltage levels seen from the AC terminal of an observed leg, however, at the expense of hindering the quality of the leg DC voltage component [8].

The converter depicted in **Fig. 1b** comprises an arbitrary number (henceforth denoted by M) of parallel SBRs, whereas the carrier signals modulating two identically indexed SMs within two adjacent SBRs belonging to the same branch can now be displaced as

$$C^{(i)}_{\mathrm{p},k+1}(\omega_{\mathrm{c}}t) = C^{(i)}_{\mathrm{p},k}(\omega_{\mathrm{c}}t - \beta) \tag{2}$$

Additionally, the relationship between two carriers modulating identically indexed SMs within two SBRs belonging to the upper and lower branch can be established as

$$C^{(i)}_{\mathrm{p},k}(\omega_{\mathrm{c}}t) = C^{(i)}_{\mathrm{n},k}(\omega_{\mathrm{c}}t - \delta) \tag{3}$$

Compared to the conventional MMC, the additional degree of freedom referring to the displacement among the SBR carrier sets, denoted by β, provides new possibilities with respect to shaping of the converter voltage content. Notice that **Fig. 1b** contains a simple illustration of the angles definition provided so far. It is noteworthy that, even if only two branches per leg are considered (the regular MMC), effects of various carrier positions depend on the parity of the number of SMs per branch [8]. With addition of parallel SBRs into the system, the number of possible combinations increases. Consequently, effects achieved by utilizing the carrier positioning degrees of freedom should be further investigated to come up with a strategy ensuring a reduction in the Total Harmonic Distortion (THD) of voltage seen from either of the chosen converter terminals.

III. Assumptions and Adopted Simplifications

In an MMC relying on the use of PSC modulation, the same modulation index is passed to all the SMs within an observed branch. Since all the SMs share the same current, while synthesizing the same fundamental voltage components, power oscillations at their terminals are ideally identical should carrier frequency be properly selected [8]. Therefore, all the SMs experience the same low frequency voltage oscillations across their capacitors. However, not all the SMs are identical in practice. Consequently, the local SM balancing [10], implying corrections of modulation index on the SM level, must be used, otherwise, individual SM voltages become unbalanced showing the tendency of diverging from their mean values over time. Nevertheless, these corrections should not corrupt the branch terminals voltage to an unacceptable extent, therefore they are normally negligible compared to initially provided modulation index reference. Consequently, $(\forall i \in [1, N])\ m_i(t) = m^*(t)$. Further, according to [7], paralleling of the SBRs, presented in **Fig. 1b**, requires corrections of modulation index corrections ($\Delta m_{\{\mathrm{p/n}\}}$) on the SBR level to be performed. Nonetheless, these corrections can be considered negligible during the forthcoming analyses. Thus, the assumption of all the SMs receiving the same modulation index remains valid. Yet, one should always be aware of the practical importance the corrections performed on the SBR/SM level have in the MMC control.

Phase-shift among the carriers within the same branch ($\gamma_{\mathrm{c}} = 2\pi/N$) causes all the SMs to switch at different time instants. Hence, their capacitor voltages are not exactly the same. Nevertheless, capacitor voltage differences refer to the oscillations occurring predominantly at high frequencies, which are successfully constrained by the proper sizing of SM capacitance [11], [12]. Thus, claiming that $v_{\mathrm{C},k}(t) \approx v_{\mathrm{C}}(t)$ can be considered a reasonable approximation.

Another observation relevant for the scope of this paper refers to the oscillations of SM voltages. Namely, every branch receives the reference voltage $v^*_{\{\mathrm{n/p}\}} = V^*_{\mathrm{br}}\left(\frac{1}{2} \pm \frac{\hat{m}}{2}\cos(\omega_{\mathrm{o}}t)\right)$ [13], where V^*_{br} denotes the reference of the total branch voltage average value, which is assumed to be properly maintained through the control of branch energies. At this point, one might expect to obtain the modulation index as

$$m^*_{\{\mathrm{n/p}\}} = \frac{v^*_{\{\mathrm{n/p}\}}}{V^*_{\mathrm{br}}} = \frac{1}{2} \pm \frac{\hat{m}}{2}\cos(\omega_\mathrm{o} t) \tag{4}$$

However, as the total branch voltages $v_{\{\mathrm{p/n}\}\Sigma}$ oscillate [12], it can be shown that the use of (4) causes the voltage produced by the branch to contain all the harmonics present in $v_{\{\mathrm{p/n}\}\Sigma}$. This method of generating the modulation index references is known as the direct modulation [14]. Even though it features global asymptotic stability, unless the additional controllers are employed, poor energy control dynamics is obtained [13], [15], [16]. Therefore, closed-loop control [17], implying modifications of modulation indices is adopted as (5) in case lower branch of the converter is observed.

$$m_\Sigma(t) = \underbrace{\left(\frac{1}{2} + \frac{\hat{m}}{2}\cos(\omega_\mathrm{o} t)\right)}_{m^*(t)} \cdot \underbrace{\frac{V^*_{\mathrm{br}}}{v_{\mathrm{br}\Sigma}(t)}}_{\alpha} \tag{5}$$

Normally, analyses of the modulation possibilities offered by any converter require the assumption of a certain operating point along with the knowledge of the modulation index used to reach it. The averaged MMC model, thoroughly explained in [18], provides a straightforward calculation of the total branch voltage oscillations, allowing for the modulation index $m_\Sigma(t)$ to be obtained in any of the reachable operating points. Further, comparison of an arbitrary reference signal $m_\Sigma(t)$ with a triangular carrier results in a pulse train $p(t)$, meaning that voltage across the terminals of an arbitrary SM equals

$$v_{\mathrm{SM}}(t) = p(t)\frac{v_{\mathrm{br}\Sigma}}{N} \tag{6}$$

It is clear from (6) that deeper analysis of the converter voltage components requires the knowledge on the SM switching function $p(t)$ to be obtained. As the total branch voltage $v_{\mathrm{br}\Sigma}$ comprises the oscillations at multiples of the converter AC currents frequency, so does the modulation index obtained as (5). **Fig. 2** depicts the modulation index time and frequency domain images for the converter operating with the parameters from **Tab. I**. When compared with direct modulation (m^*), closed-loop control of the MMC (m_Σ) introduces additional harmonics into the modulation index. Hence (7) can be established should the most dominant components observed in the frequency domain image of m_Σ be taken into account.

$$\begin{aligned} m_\Sigma(t) \approx m_0 + \hat{m}_1\cos(\omega_\mathrm{o} t + \zeta_1) + \\ \hat{m}_2\cos(2\omega_\mathrm{o} t + \zeta_2) + \hat{m}_3\cos(3\omega_\mathrm{o} t + \zeta_3) \end{aligned} \tag{7}$$

TABLE I: Parameters of the converter utilized for verification of the expressions derived herewith

Parameter	Label	Value
Rated power	P	1MW
DC link voltage	V_{in}	5.5kV
AC grid voltage	v_g	3.3kV
Number of SMs per SBR	N	8
Number of SBRs per branch	M	2
SM capacitance	C_{SM}	2.25mF
SBR inductance	L_{br}	5mH
SM switching frequency	f_c	285Hz
Grid inductance	L_g	3.47mH

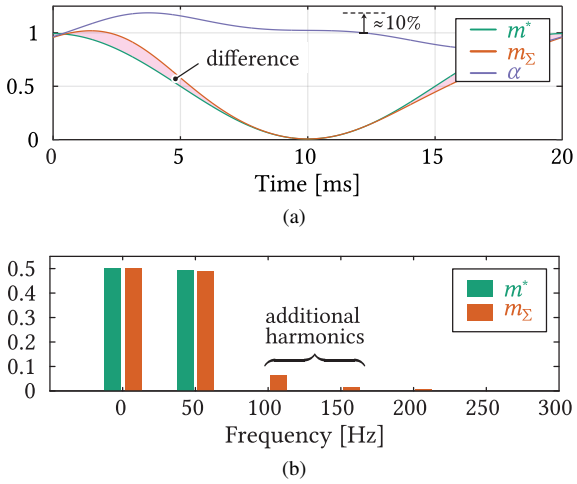

Fig. 2. Modulation index obtained in the manner characterizing the MMC closed loop control in both time domain (top plot) and frequency domain (bottom plot).

In [19], [20] a systematic approach towards deriving the spectrum of a Pulse-Width Modulation (PWM) pulse train was presented. It relies on the use of 1-D functions to obtain the results already presented in [21], however, without the need for utilizing the so-called double Fourier integrals. Having adopted all of the above assumptions and after a set of mathematical manipulations, one can obtain the SM switching function of an arbitrary SM as

$$\begin{aligned} p(t) = m(t) + \frac{2}{\pi}\sum_{k=1}^{\infty}\sum_{z=-\infty}^{\infty}\sum_{q=-\infty}^{\infty}\sum_{n=-\infty}^{\infty}\frac{(-1)^k}{k}\times \\ J_z(k\pi\hat{m}_3)J_q(k\pi\hat{m}_2)J_n(k\pi\hat{m}_1)\sin(k\pi m_0 + \frac{z+q+n}{2}\pi)\times \\ \cos([k\omega_c + (3z+2q+n)\omega_\mathrm{o}]t - k\gamma_\mathrm{c} + (z\zeta_3 + q\zeta_2 + n\zeta_1)), \end{aligned} \tag{8}$$

where $J_n(x)$ denotes the Bessel function of the first kind.

IV. Analysis of Voltage Components Generated by the Converter Leg

A. SBR voltage analysis

To obtain the SBR voltage, summation of expressions (8) written for every individual SM can be performed as (9). Without the loss of generality, SBRs belonging to the lower branch of the converter phase A will be observed.

$$v_{\mathrm{SBR}} = \sum_{i=1}^{N} v_{\mathrm{SM},i} \tag{9}$$

By adopting $\gamma_\mathrm{c}(i) = (i-1)2\pi/N$, while noticing that none of the Bessel functions from (8) depends on the summation index i, leads to (10). Notice that the sideband harmonics, which are defined as components for which $\omega_{zqn} \neq 0$ in the SBR voltage spectrum, appear around the multiples of $\omega_{\mathrm{SBR}} = N\omega_\mathrm{c}$. Thus, ω_{SBR} is referred to as the SBR apparent switching frequency.

$$v_{\mathrm{SBR}} = \underbrace{m^* V_{\mathrm{br}}^*}_{v_{\mathrm{n}}^*} + \frac{2v_{\mathrm{n}\Sigma}}{\pi N}\sum_{r=1}^{\infty}\sum_{z=-\infty}^{\infty}\sum_{q=-\infty}^{\infty}\sum_{n=-\infty}^{\infty}\frac{1}{r}J_z(rN\pi\hat{m}_3)\times$$
$$J_q(rN\pi\hat{m}_2)J_n(rN\pi\hat{m}_1)\sin\left(rN\pi\underbrace{(m_0-1)}_{\approx-\frac{1}{2}}+\frac{z+q+n}{2}\pi\right)\times$$
$$\cos([r\underbrace{N\omega_c}_{\omega_{\mathrm{SBR}}}+\underbrace{(3z+2q+n)\omega_{\mathrm{o}}}_{\omega_{zqn}}]t+\underbrace{z\zeta_3+q\zeta_2+n\zeta_1}_{\theta_{zqn}}) \tag{10}$$

Calculation of the SBR voltage according to (10) introduces the need to represent the SBR total voltage according to (11). The oscillating components' magnitudes ($\Delta\hat{v}_1$ and $\Delta\hat{v}_2$), along with their phase angles (Ψ_1 and Ψ_2), can be obtained from the branch averaged models [18].

$$v_{\{\mathrm{p/n}\}\Sigma} = V_{\mathrm{br}}^* \pm \overbrace{\Delta\hat{v}_1\cos(\omega t+\Psi_1)}^{\Delta v_1^{\sim}} - \overbrace{\Delta\hat{v}_2\cos(\omega t+\Psi_2)}^{\Delta v_2^{\sim}} \tag{11}$$

In order to verify the effectiveness of (10), the averaged simulation model of the MMC with parameters provided in **Tab. I** was developed in PLECS. In accordance with the converter averaged model presented in [18], the steady state currents and voltages were calculated under the assumption of the converter delivering the rated power to the grid with unity power factor. Thereafter, these were used with the aim of calculating the branch energy (voltage) variations. As can be seen from **Fig. 3**, an excellent matching of the spectral contents of the SBR voltage obtained with (10) and PLECS simulations can be observed.

THD, defined in (12), represents a common way of expressing the amount of higher order harmonics within a certain waveform. By combining (10) and (12) in MATLAB, THD of the SBR voltage, under the conditions defined in **Tab. I**, was estimated as $\mathrm{THD}_{\mathrm{calc}} = 13.48\%$.

$$\mathrm{THD} = \frac{1}{\hat{v}_1}\sqrt{\sum_{i=2}^{N}\hat{v}_{\mathrm{i}}^2} \tag{12}$$

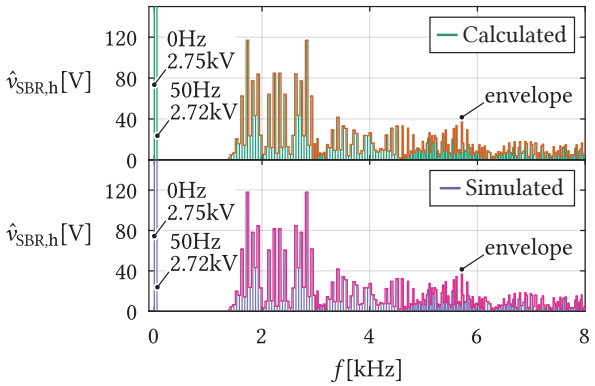

Fig. 3. Comparison between the SBR spectral contents obtained from the analytic expressions (10) and (11) and simulations. For the sake of alleviating the comparison in the visual sense, envelopes of both spectral contents are provided. Since fundamental and DC components of voltage generated by a SBR are not in the focus of this paper, the scale was adjusted such that higher order harmonics can be presented to the best possible extent.

Also, THD relative error provides an illustrative gauge of the mismatch between the simulated and calculated spectra and in the case depicted in **Fig. 3** it was calculated as $\Delta\mathrm{THD}_{\%} = -0.77\%$. Consequently, the assumptions introduced in **Sec. III** do not contribute to severe errors when considering the possible reductions in the converter AC voltage components. Additionally, it can be seen from both plots in **Fig. 3** that the first set of harmonics indeed appears centered around the SBR apparent switching frequency, which in the analyzed case equals 2280Hz. As will be demonstrated shortly, introducing a proper time shift in the switching events of parallel SBRs ensures cancellation of this harmonics set.

The switched model of the converter, with parameters provided in **Tab. I**, was created in PLECS to present the time domain voltages generated by the analyzed converter parts. **Fig. 4** presents one period of voltage generated by the SBR analyzed above.

B. Branch voltage analysis

In case M SBRs are connected in parallel, and without any SMs being temporarily/permanently bypassed (i.e. no faulty SMs), the equivalent voltage seen from the lower branch terminals can be expressed as (13).

$$v_{\mathrm{n}} = \frac{1}{M}\sum_{j=1}^{M} v_{\mathrm{SBR,j}} \tag{13}$$

As defined in **Sec. II**, the sets of carriers utilized to modulate two adjacent SBRs can be shifted by an angle denoted by β. On these terms, substitution of (10) into (13), followed by a set of tedious mathematical manipulations, provides

$$v_{\mathrm{n}} = v_{\mathrm{n}}^* + \frac{2v_{\mathrm{n}\Sigma}}{\pi NM}\sum_{u=1}^{M}\sum_{i=1}^{N}\sum_{k=1}^{\infty}\sum_{z=-\infty}^{\infty}\sum_{q=-\infty}^{\infty}\sum_{n=-\infty}^{\infty}\frac{(-1)^k}{k}\times$$
$$J_z(k\pi\hat{m}_3)J_q(k\pi\hat{m}_2)J_n(k\pi\hat{m}_1)\sin(k\pi m_0+\frac{z+q+n}{2}\pi)\times$$
$$\cos([k\omega_c+\omega_{zqn}]t-k\left[(i-1)\frac{2\pi}{N}+(u-1)\beta\right]+\theta_{zqn}) \tag{14}$$

By carefully analyzing (14) one can conclude that if $\beta = 2\pi/(MN)$ holds, (15) follows directly from (14). It is noteworthy that such a selection of the angle β causes the apparent switching frequency of the branch ω_{BR} to increase

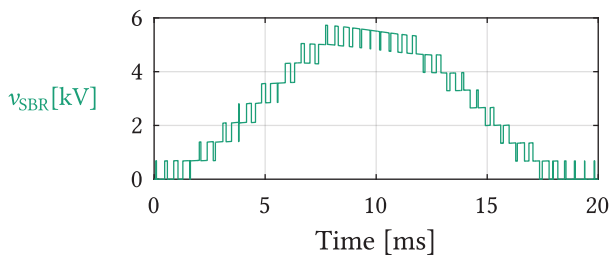

Fig. 4. Voltage produced by the SBR analyzed throughout this subsection. Since shifting the carriers within an observed SBR causes its SMs to switch at different time instants, up to $N+1$ voltage levels can be observed.

M times compared to the apparent switching frequency of a single SBRs. For the purpose of validating the correctness of (15), PLECS simulations of the converter with parameters provided in **Tab. I** were reused. **Fig. 5** presents the branch voltage spectral components obtained by means of analytic expressions and simulations. With the aim of emphasizing the effect of shifting the carrier sets modulating two adjacent SBRs, the spectral components of an individual SBR voltage (from **Fig. 3**) were intentionally included and shown in the background (gray curves).

$$v_{\mathrm{n}} = v_{\mathrm{n}}^{*} + \frac{2v_{\mathrm{n}\Sigma}}{\pi NM}\sum_{p=1}^{\infty}\sum_{z=-\infty}^{\infty}\sum_{q=-\infty}^{\infty}\sum_{n=-\infty}^{\infty}\frac{1}{p}J_z(pMN\pi\hat{m}_3)\times$$
$$J_q(pMN\pi\hat{m}_2)J_n(pMN\pi\hat{m}_1)\sin\Bigg(pMN\pi\underbrace{(m_0-1)}_{\approx\frac{1}{2}}+$$
$$\underbrace{\frac{z+q+n}{2}\pi}_{\Phi_{zqn}}\Bigg)\cos(\underbrace{[pMN\omega_c}_{\omega_{\mathrm{br}}}+\omega_{zqn}]t+\theta_{zqn}) \tag{15}$$

In contrast to the SBR voltage, the branch voltage does not contain any spectral components centered around the SBR apparent switching frequency. Conversely, all the sideband harmonics are centered around the branch apparent switching frequency ω_{BR}, which in the analyzed case equals $\omega_{\mathrm{BR}} = 4560\mathrm{Hz}$. As a result, the branch voltage THD, calculated as $\mathrm{THD}_{\mathrm{calc}} = 6.58\%$, gets approximately halved when compared to the THD of an individual SBR. To estimate the correctness of the results obtained by means of (15), the relative THD error was calculated as $\Delta\mathrm{THD}_{\%} = 0.64\%$. Thus, an excellent matching between the simulated and calculated branch voltage spectrum is achieved.

Fig. 6 depicts time domain waveform of the analyzed branch voltage obtained through the switched model of the converter. As can be seen, the above mentioned spectral components cancellation manifests through an increase in the number of voltage levels $(MN+1)$ compared to a single SBR voltage $(N+1)$. As reduced voltage steps can be observed in the branch voltage waveform, THD reduction becomes logical and intuitive.

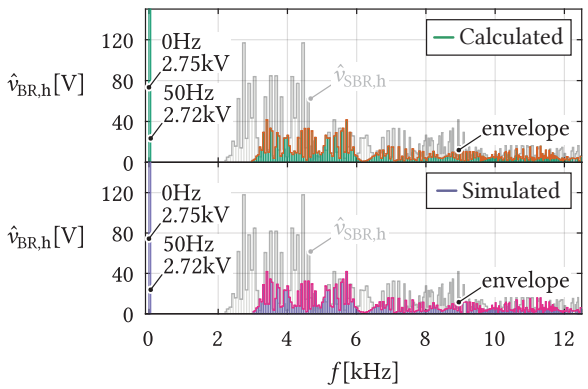

Fig. 5. Comparison between the branch spectral contents obtained from the analytic analysis (15) and the simulations. To emphasize the change in the branch voltage, an individual SBR voltage spectrum ($\hat{v}_{\mathrm{BR,h}}$) was intentionally included and colored in gray.

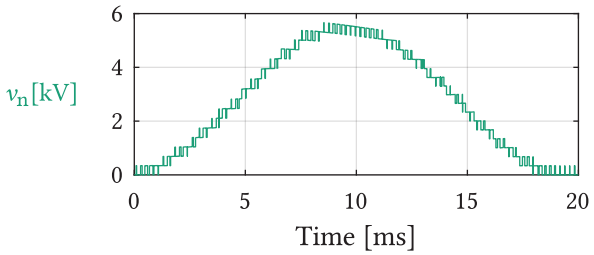

Fig. 6. Voltage produced by the branch analyzed throughout this subsection. The number of voltage levels observed from the branch terminals gets increased $(MN+1)$ compared to the case assuming a single SBR $(N+1)$.

C. Leg voltage analysis

Two voltage components being relevant for the MMC leg can be calculated as $v_{\{\mathrm{c/s}\}} = (v_{\mathrm{n}} \pm v_{\mathrm{p}})/2$, where v_{c} and v_{s} denote the DC and AC voltage components, respectively. Derivation of the upper branch voltage starts with an arbitrary SBR belonging to it, similarly to (10). However, there are two differences with respect to (10). Firstly, observation of (16) and (17) shows that all the components oscillating at ω_{o} in m_{n} and m_{p} are in the counter phase, whereas the opposite is claimed for the components oscillating at $2\omega_{\mathrm{o}}$. Thus, it is logical to state that the same applies to the spectral components of their Fourier transformations, leading to (18) and (19).

$$m_{\mathrm{n}} = \frac{\left\{\frac{1}{2}+\frac{\hat{m}}{2}\cos(\omega_{\mathrm{o}}t)\right\}V_{\mathrm{br}}^{*}}{V_{\mathrm{br}}^{*}-\Delta\hat{v}_1\cos(\omega_{\mathrm{o}}+\Psi_1)-\Delta\hat{v}_2\cos(2\omega_{\mathrm{o}}+\Psi_2)} \tag{16}$$

$$m_{\mathrm{p}} = \frac{\left\{\frac{1}{2}-\frac{\hat{m}}{2}\cos(\omega_{\mathrm{o}}t)\right\}V_{\mathrm{br}}^{*}}{V_{\mathrm{br}}^{*}+\Delta\hat{v}_1\cos(\omega_{\mathrm{o}}+\Psi_1)-\Delta\hat{v}_2\cos(2\omega_{\mathrm{o}}+\Psi_2)} \tag{17}$$

$$\{m_{\mathrm{p0}},\hat{m}_{\mathrm{p1}},\hat{m}_{\mathrm{p2}},\hat{m}_{\mathrm{p3}}\} = \{m_{\mathrm{n0}},\hat{m}_{\mathrm{n1}},\hat{m}_{\mathrm{n2}},\hat{m}_{\mathrm{n3}}\} \tag{18}$$

$$\{\zeta_{\mathrm{p1}},\zeta_{\mathrm{p2}},\zeta_{\mathrm{p3}}\} = \{\zeta_{\mathrm{n1}}-\pi,\zeta_{\mathrm{p2}},\zeta_{\mathrm{p3}}-\pi\} \tag{19}$$

Secondly, according to (1), the upper branch carrier sets can be shifted with respect to their bottom branch counterparts by an angle δ, leading to (20), where $v_{\mathrm{p}}^{*} = V_{\mathrm{br}}^{*}\left(\frac{1}{2}-\frac{\hat{m}}{2}\cos(\omega_{\mathrm{o}})\right)$.

$$v_{\mathrm{p}} = v_{\mathrm{p}}^{*} + \frac{2v_{\mathrm{p}\Sigma}}{\pi MN}\sum_{p=1}^{\infty}\sum_{z=-\infty}^{\infty}\sum_{q=-\infty}^{\infty}\sum_{n=-\infty}^{\infty}\frac{1}{p}J_z(pMN\pi\hat{m}_3)$$
$$J_q(pMN\pi\hat{m}_2)J_n(pMN\pi\hat{m}_1)\sin(\Phi_{zqn}-\frac{pMN\pi}{2})$$
$$\cos(\underbrace{[pMN\omega_c+\omega_{zqn}]}_{\omega_{pzqn}}t-(pMN\delta+(n+z)\pi)+\theta_{zqn}) \tag{20}$$

The AC voltage of the observed leg can be calculated as $v_{\mathrm{s}} = (v_{\mathrm{n}} - v_{\mathrm{p}})/2$, whereas correct derivation of its spectral components, whilst utilizing previously derived results, requires the total SBR voltages to be expressed in their complete form (11). To make the following analyses more lucid, branch voltages can be expressed as

$$v_{\mathrm{n}} = v_{\mathrm{n}}^{*} + g_{\mathrm{h,n}}(\omega) v_{\mathrm{n}\Sigma} \tag{21}$$

$$v_{\mathrm{p}} = v_{\mathrm{p}}^{*} + g_{\mathrm{h,p}}(\omega) v_{\mathrm{p}\Sigma}, \tag{22}$$

which yields

$$v_{\mathrm{s}} = \underbrace{\hat{m}\frac{V_{\mathrm{br}}^{*}}{2}\cos(\omega_{\mathrm{o}} t)}_{\text{fundamental component}} + \frac{V_{\mathrm{br}}^{*}}{2}\left[g_{\mathrm{h,n}}(\omega) - g_{\mathrm{h,p}}(\omega)\right] - \frac{\Delta v_1^{\sim}}{2}\left[g_{\mathrm{h,n}}(\omega) + g_{\mathrm{h,p}}(\omega)\right] - \frac{\Delta v_2^{\sim}}{2}\left[g_{\mathrm{h,n}}(\omega) - g_{\mathrm{h,p}}(\omega)\right] \tag{23}$$

Similarly, the leg DC voltage can be obtained as

$$v_{\mathrm{c}} = \underbrace{\frac{V_{\mathrm{br}}^{*}}{2}}_{\text{DC value}} + \frac{V_{\mathrm{br}}^{*}}{2}\left[g_{\mathrm{h,n}}(\omega) + g_{\mathrm{h,p}}(\omega)\right] - \frac{\Delta v_1^{\sim}}{2}\left[g_{\mathrm{h,n}}(\omega) - g_{\mathrm{h,p}}(\omega)\right] - \frac{\Delta v_2^{\sim}}{2}\left[g_{\mathrm{h,n}}(\omega) + g_{\mathrm{h,p}}(\omega)\right] \tag{24}$$

An interesting fact regarding the terms describing the higher order harmonics can be observed from (23) and (24). Namely, the terms in the brackets multiplying the same voltage components have the opposite signs. This indicates that cancellation of a certain harmonic group in the AC voltage doubles the same frequency component in the DC voltage of an observed leg and vice versa. Thus, there is a certain trade-off that needs to be considered and treated accordingly. To commence the analysis on the possible use of the lower and upper branch carrier sets displacement (δ), let one expand $g_{\mathrm{h,n}}(\omega) - g_{\mathrm{h,p}}(\omega)$ as (25), where $\delta = \alpha\pi/(MN)$ was adopted.

$$g_{\mathrm{h,n}}(\omega) - g_{\mathrm{h,p}}(\omega) = \frac{2}{\pi MN} \times \sum_{p=1}^{\infty}\sum_{z=-\infty}^{\infty}\sum_{q=-\infty}^{\infty}\sum_{n=-\infty}^{\infty}\frac{1}{p} J_z(pMN\pi\hat{m}_3) J_q(pMN\pi\hat{m}_2) \times J_n(pMN\pi\hat{m}_1)\sin(\Phi_{zqn} - \frac{pMN\pi}{2})\cos(\omega_{pzqn}t + \theta_{zqn}) \times \underbrace{\left(1 + (-1)^{q+p(\alpha+MN)}\right)}_{\Delta_{\mathrm{AC}}} \tag{25}$$

From (25) the dependency $\Delta_{\mathrm{AC}} = f(p, q, \alpha)$ is revealed. Further analysis referring to the minimization of the leg AC voltage spectrum requires one to assign some discrete values to indices p and q. According to **Fig. 5**, the first group of harmonics observed in the branch voltage spectrum appears around the apparent switching frequency of the branch. Therefore, cancellation of this harmonics set clearly contributes to the reduction of the leg AC voltage THD. Hence, p can be set as unity. For a fixed p, the Bessel function $J_q(pMN\pi\hat{m}_2)$ reaches its maximum for $q = 0$. Consequently, the cancellation of harmonics for which $p = 1$ and $q = 0$, formulated as $\Delta_{\mathrm{AC}}|_{\{p,q\}=\{1,0\}} = 0$, is expected to lead towards meeting the criteria of the lowest leg AC voltage THD. In order to satisfy $\Delta_{\mathrm{AC}}|_{\{p,q\}=\{1,0\}} = 0$, the term $\alpha + MN$ must be odd and values of the angle δ (please, recall that $\delta = \alpha\pi/MN$) allowing for this goal to be obtained are presented in **Tab. II**.

TABLE II: Values of the angle δ leading to the desired cancelation of carrier harmonics seen from the converter AC terminals

N \ M	odd	even
odd	$\delta = 0$	$\delta = \frac{\pi}{MN}$
even	$\delta = \frac{\pi}{NM}$	$\delta = \frac{\pi}{NM}$

To check the effects of the AC voltage THD improvement upon the leg DC voltage component, the term Δ_{DC}, given in (26), can be used. Please notice that $\Delta_{\mathrm{DC}} + \Delta_{\mathrm{AC}} = 2$ holds.

$$\Delta_{\mathrm{DC}} = 1 - (-1)^{q+p(\alpha+MN)} \tag{26}$$

The cancellation of spectral components centered around the branch apparent switching frequency can be conducted by following the already presented logic, which ultimately results in **Tab. III**. In order to validate the correctness of the analytic expressions derived throughout this section, **Figs. 7** and **8** present the comparison between the spectral contents of the leg voltage components obtained in the analytic fashion and simulations conducted in PLECS. Once again, the converter with parameters defined in **Tab. I** was simulated. **Fig. 7** presents the spectrum of both AC and DC voltage components of the observed converter in case $\delta = 0$. By comparing the plots within the figure, one can conclude that an outstanding matching between the harmonic values obtained by calculations and simulations tool is achieved. As the functionality of analytic expressions derived above is confirmed, the analysis of the effect obtained by setting the angle δ (phase-shift between upper and lower branch carrier sets) to a non-zero value can be conducted.

From **Fig. 8a** it can be seen that, when compared with **Fig. 7a**, the density of the components centered around the branch apparent switching frequency gets reduced. In turn, these get shifted to the DC side as can be seen through the comparison of **Figs. 7b** and **8b**. To provide a quantitative comparison between **Figs. 7a** and **8a**, THD was calculated according to (12) for both cases and results can be found summarized in **Tab. IV**. As expected, the leg AC voltage THD gets reduced with the introduction of non-zero displacement between the branch carrier sets. The opposite applies to the leg DC voltage THD. Also, the relative error of both THD components confirms that excellent matching between the analytic and simulation results is retained. It is noteworthy that, although uncommon, THD of the leg DC voltage was defined as (27) in order to provide the means for comparison of spectral contents obtained by using different values of δ.

$$\mathrm{THD}_{\mathrm{DC}} = \frac{1}{V_{\mathrm{br}}^{*}}\sqrt{\sum_{i=1}^{\infty}\hat{v}_{\mathrm{c},i}^{2}} \tag{27}$$

TABLE III: Values of the angle δ leading to the desired cancelation of carrier harmonics seen from the converter DC terminals

N \ M	odd	even
odd	$\delta = \frac{\pi}{NM}$	$(\delta = 0) \vee (\delta = \pi)$
even	$(\delta = 0) \vee (\delta = \pi)$	$(\delta = 0) \vee (\delta = \pi)$

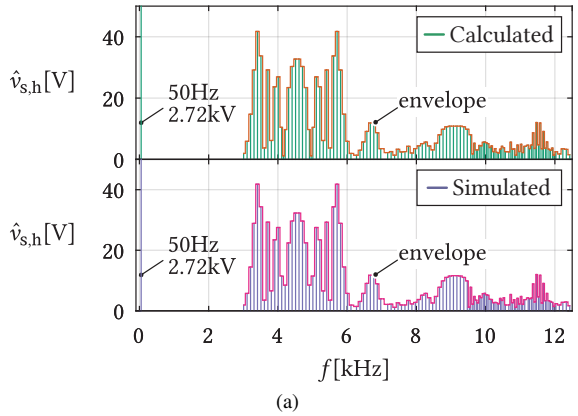

Fig. 7. Comparison of leg AC (left) and DC (right) voltage spectral contents obtained by means of analytic expression and averaged simulation model in case $\delta = 0$. According to **Tab. I**, $N = 8$ and $M = 2$.

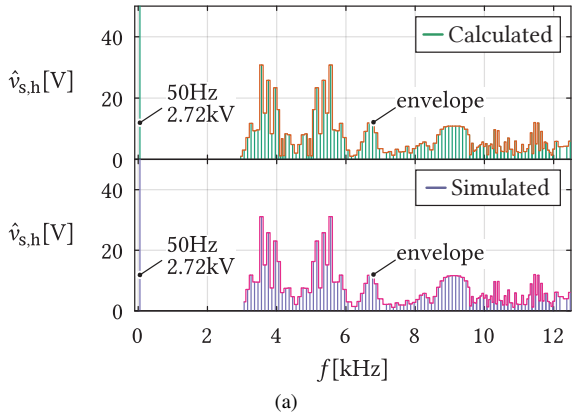

Fig. 8. Comparison of leg AC (left) and DC (right) voltage spectral contents obtained by means of analytic expression and averaged simulation model in case $\delta = \pi/MN$. According to **Tab. I**, $N = 8$ and $M = 2$, therefore $\delta = 11.25°$.

Last but not least, the question on whether the phase shifts provided in **Tabs. II** and **III** are indeed optimal, meaning that they lead to the highest possible minimization of THD at either of the chosen leg sides, remains open. In order to provide the proof regarding the validity of conclusions drawn during the derivation of **Tabs. II** and **III**, THD was calculated for both AC and DC voltage, with the angle δ being swept from 0 to $2\pi/MN$. **Fig. 9a** presents the change in the leg voltage components THD in case the converter parameters are unchanged with respect to all the cases analyzed throughout this section. Therefore, as $M = 2$ and $N = 8$, the product MN is even. It can be noticed that the leg AC voltage THD decreases until δ reaches the value corresponding to $\pi/MN \leftrightarrow 11.25°$. Please, notice the correspondence to **Tab. II**. On the other hand, the lowest value of $\mathrm{THD}_{\mathrm{DC}}[\%]$ is observed in case $\delta = 0$, confirming the correctness of information provided in **Tab. III**. In contrast to the case considering the product MN being even, **Fig. 9b** presents the same THD components in case the converter operates with the same voltages and currents taken into account so far, however, with $M = 3$ and $N = 7$. As the displacement δ increases, so does the THD of the leg AC voltage component, which is aligned with the proposal

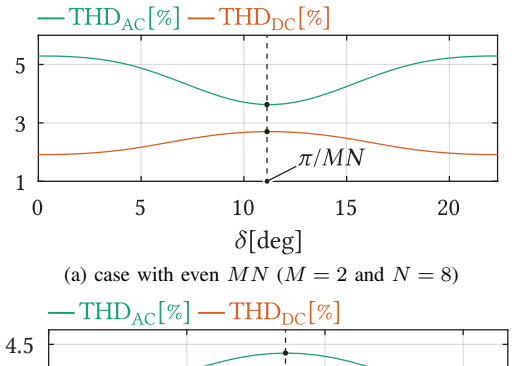

(a) case with even MN ($M = 2$ and $N = 8$)

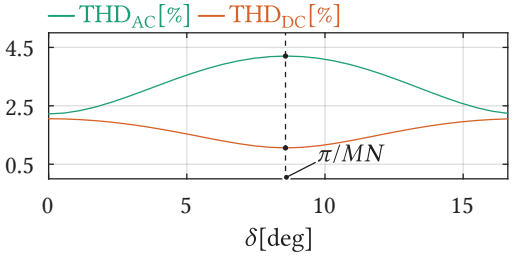

(b) case with odd MN ($M = 3$ and $N = 7$)

Fig. 9. Variation of the leg voltage components THD depending on the value of branch carrier sets displacement.

TABLE IV: THD values for two different values of branch carrier sets shifts

δ	$\mathrm{THD}_{\mathrm{AC}}[\%]$	$\mathrm{THD}_{\mathrm{DC}}[\%]$	$\Delta\mathrm{THD}_{\mathrm{AC}}[\%]$	$\Delta\mathrm{THD}_{\mathrm{DC}}[\%]$
0	5.29	1.92	0.36	0.19
$\pi/16$	3.62	2.70	0.33	0.27

of δ from **Tab. II**. Additionally, once δ reaches π/MN, the leg DC voltage THD reaches its minimum, which is expected should **Tab. III** be observed. Consequently, the logic presented throughout this paper ensures the highest possible reduction in the THD seen from any of the chosen converter ports.

V. Conclusion

Apart from allowing for an effortless extension of the MMC power capacity, paralleling of its branches offers the outstanding flexibility when it comes to sythetization of its reference voltages. When compared to the conventional MMC, additional degrees of freedom from the modulation standpoint are introduced. Therefore, the MMC utilizing parallel SBRs features the extended possibilities of shaping the voltage created across its terminals when compared to its conventional counterpart. Throughout this paper, detailed mathematical analysis on the possibilities offered by the use of PSC modulation within the converter operating with an arbitrary number of SBRs, comprising an arbitrary number of SMs, was conducted. Moreover, this work incorporates the corrections of modulation index, characterizing the MMC closed loop control, into the analysis making it unique and different compared to the existing references, which focus mainly on the operation implying the so-called direct modulation. As it was shown, a suitable choice in the angular displacement between the sets of carriers modulating two opposite branches of the same leg, leads to the reduction of THD at either DC or AC port of the converter. Nevertheless, there is always a trade-off which one must be aware of. In other words, reduction of the AC voltage THD implies shifting of a certain part of its spectral energy (more precisely, the one being related to the higher frequencies) to the DC side. The conclusion in the opposite direction, of course, holds as well.

References

[1] J. Gerdes, "Siemens debuts hvdc plus with san francisco's trans bay cable," *Living Energy*, vol. 5, pp. 28–31, 2011.

[2] H. Knaak, "Modular multilevel converters and hvdc/facts: A success story," in *Proceedings of the 2011 14th European Conference on Power Electronics and Applications*, Aug. 2011, pp. 1–6.

[3] M. Winkelnkemper, A. Korn, and P. Steimer, "A modular direct converter for transformerless rail interties," in *2010 IEEE International Symposium on Industrial Electronics*, Jul. 2010, pp. 562–567.

[4] T. J. Hammons, V. F. Lescale, K. Uecker, M. Haeusler, D. Retzmann, K. Staschus, and S. Lepy, "State of the art in ultrahigh-voltage transmission," *Proceedings of the IEEE*, vol. 100, no. 2, pp. 360–390, Feb. 2012.

[5] *Changji-guquan UHVDC link*.

[6] M. Basic, P. C. Silva, and D. Dujic, "High power electronics innovation perspectives for pumped storage power plants," 2018.

[7] S. Milovanović and D. Dujić, "On facilitating the modular multilevel converter power scalability through branch paralleling," in *2019 IEEE Energy Conversion Congress and Exposition (ECCE)*, Sep. 2019.

[8] K. Ilves, L. Harnefors, S. Norrga, and H. Nee, "Analysis and operation of modular multilevel converters with phase-shifted carrier pwm," *IEEE Transactions on Power Electronics*, vol. 30, no. 1, pp. 268–283, Jan. 2015.

[9] B. Li, R. Yang, D. Xu, G. Wang, W. Wang, and D. Xu, "Analysis of the phase-shifted carrier modulation for modular multilevel converters," *IEEE Transactions on Power Electronics*, vol. 30, no. 1, pp. 297–310, Jan. 2015.

[10] M. Hagiwara and H. Akagi, "Control and experiment of pulsewidth-modulated modular multilevel converters," *IEEE Transactions on Power Electronics*, vol. 24, no. 7, pp. 1737–1746, Jul. 2009.

[11] K. Ilves, S. Norrga, L. Harnefors, and H. Nee, "On energy storage requirements in modular multilevel converters," *IEEE Transactions on Power Electronics*, vol. 29, no. 1, pp. 77–88, Jan. 2014.

[12] M. Vasiladiotis, N. Cherix, and A. Rufer, "Accurate capacitor voltage ripple estimation and current control considerations for grid-connected modular multilevel converters," *IEEE Transactions on Power Electronics*, vol. 29, no. 9, pp. 4568–4579, Sep. 2014.

[13] L. Harnefors, A. Antonopoulos, S. Norrga, L. Angquist, and H. Nee, "Dynamic analysis of modular multilevel converters," *IEEE Transactions on Industrial Electronics*, vol. 60, no. 7, pp. 2526–2537, Jul. 2013.

[14] K. Sharifabadi, L. Harnefors, H.-P. Nee, S. Norrga, and R. Teodorescu, *Design, control, and application of modular multilevel converters for HVDC transmission systems*. John Wiley & Sons, 2016.

[15] S. Cui, J. Jung, Y. Lee, and S. Sul, "Principles and dynamics of natural arm capacitor voltage balancing of a direct modulated modular multilevel converter," in *2015 9th International Conference on Power Electronics and ECCE Asia (ICPE-ECCE Asia)*, Jun. 2015, pp. 259–267.

[16] L. Harnefors, A. Antonopoulos, K. Ilves, and H. Nee, "Global asymptotic stability of current-controlled modular multilevel converters," *IEEE Transactions on Power Electronics*, vol. 30, no. 1, pp. 249–258, Jan. 2015.

[17] A. Antonopoulos, L. Angquist, and H.-P. Nee, "On dynamics and voltage control of the modular multilevel converter," in *Power Electronics and Applications, 2009. EPE'09. 13th European Conference on*, IEEE, 2009, pp. 1–10.

[18] A. F. Christe, "Galvanically isolated modular converter," p. 194, 2018.

[19] H. Mouton and B. Putzeys, "Understanding the pwm nonlinearity: Single-sided modulation," *IEEE Transactions on Power Electronics*, vol. 27, no. 4, pp. 2116–2128, Apr. 2012.

[20] H. d. T. Mouton, B. McGrath, D. G. Holmes, and R. H. Wilkinson, "One-dimensional spectral analysis of complex pwm waveforms using superposition," *IEEE Transactions on Power Electronics*, vol. 29, no. 12, pp. 6762–6778, Dec. 2014.

[21] D. G. Holmes and T. A. Lipo, *Pulse width modulation for power converters: principles and practice*. John Wiley & Sons, 2003, vol. 18.